

Nonlinear clustering during the cosmic Dark Ages and its effect on the 21-cm background from minihalos

Ilian T. Iliev,¹ Evan Scannapieco,¹ Hugo Martel,² and Paul R. Shapiro²

¹ *Osservatorio Astrofisico di Arcetri, Largo Enrico Fermi 5, 50125 Firenze, Italy*

² *Department of Astronomy, University of Texas, Austin, TX 78712-1083*

2 December 2024

ABSTRACT

Hydrogen atoms inside virialized minihalos (with $T_{\text{vir}} \leq 10^4 \text{K}$) before and during reionization create a radiation background from redshifted 21-cm line emission whose angular fluctuations reflect the clustering of halos during this early epoch. We have shown elsewhere that this effect may be detectable with the planned Low Frequency Array (LOFAR) and Square Kilometer Array (SKA) in a flat Cold Dark Matter Universe with a cosmological constant (Λ CDM). This is a direct probe of structure during the “Dark Ages” at redshifts $z \gtrsim 6$ and down to smaller scales than have previously been constrained. In our original prediction of this effect, we used a standard approximation known as the “linear bias” [e.g. Mo & White (1996)]. Here we improve upon that treatment by considering the effect of nonlinear clustering. To accomplish this, we develop a new analytical method for calculating the nonlinear Eulerian bias of halos, which should be useful for other applications as well. Predictions of this method are compared with the results of Λ CDM N-body simulations, showing significantly better agreement than the standard linear bias approximation. When applied to the 21-cm background from minihalos, our formalism predicts fluctuations which differ from our original predictions by up to 30% at low frequencies (high- z) and small scales. However, within the range of frequencies and angular scales at which the signal could be observable by LOFAR and SKA as currently planned, the differences are small and our original predictions prove robust. Our results indicate that observations with smaller frequency bandwidth will see a correspondingly higher signal that is more sensitive to nonlinear effects. Finally we combine the results of our N-body simulations, of a co-moving volume that contains thousands of minihalos, with our previous calculations of the 21-cm emission from individual minihalos to construct illustrative radio emission maps at redshift $z = 9$.

Key words: cosmology: theory — diffuse radiation — intergalactic medium — large-scale structure of universe — galaxies: formation — radio lines: galaxies

1 INTRODUCTION

Despite striking progress over the past decade, cosmologists have still failed to see into the “Dark Ages” of cosmic time. Although the details of this epoch between recombination at redshift $z \sim 10^3$ and reionization at $z \gtrsim 6$ are crucial for understanding issues ranging from early structure formation to the process of reionization itself, no direct observations of any kind have been made in this redshift range. Recently, we made the first proposal for such direct observations (Iliev et al. 2002, from hereafter Paper I) based on collisional excitation of the hydrogen 21-cm line in the warm, dense, neutral gas in virialized minihalos (halos with virial temperature $T_{\text{vir}} \leq 10^4 \text{K}$), the first baryonic structures to emerge in the standard CDM universe. We showed that this collisional excitation is sufficient to decouple the spin temperature of the H atoms inside minihalos from the temperature of the cosmic microwave background (CMB), with spin temperature $T_S > T_{\text{CMB}}$, in general. Minihalos should generally appear in emission with respect to the CMB, therefore, producing a radiation background of redshifted 21-cm line emission, a “21-cm forest” of redshifted emission lines, well-separated in frequency. Unlike all previous studies (Hogan & Rees

1979; Scott & Rees 1990; Subramanian & Padmanabhan 1993; Madau, Meiksen & Rees 1997; Shaver et al. 1999; Tozzi et al. 2000), this mechanism does not require sources of Ly α radiation for “pumping” the 21-cm line and decoupling it from the CMB.

In Iliev et al. (2002) we calculated the 21-cm emission properties of individual minihalos in detail, along with the total minihalo emission background and the large-scale fluctuations of this background due to clustering. Although both individual minihalo lines and the overall background are too weak to be readily detected, we found that the emission fluctuations on scales from few to ~ 100 arc min should be measurable with the currently-planned radio arrays LOFAR and SKA if sufficiently long integration times are utilized. We demonstrated that such observations can be used to probe the details of reionization as well as measure the power spectrum of density fluctuations at far smaller scales than have previously been constrained.

In the current paper we extend these results to smaller scales where the clustering of halos becomes nonlinear. Our previous calculations showed that the fluctuation signal increases as the beam size and frequency bandwidth decrease, which corresponds to sampling the 21-cm emission from minihalos within smaller volumes. These smaller scale volumes correspond in turn to length scales in the density fluctuation power spectrum that are more nonlinear at the relevant epoch. Thus nonlinear effects have the greatest impact on the angular fluctuations of the radiation background on the small angular scales and in the small frequency bandwidths at which the signal is strongest.

This issue is of particular importance as our previous investigations used the standard, simplified nonlinear bias of Mo & White (1996), which is likely to be break down at many of the relevant redshifts and length scales. For example, an rms density fluctuation in a Cold Dark Matter universe with a cosmological constant (Λ CDM) at $z = 6(8)$, is strongly nonlinear ($\sigma(M) \geq 1$) for $M \leq 10^9 M_\odot$ ($6.2 \times 10^7 M_\odot$), which roughly corresponds to the region sampled by beam sizes 9" (3"), for frequency bandwidths 12 kHz (3 kHz), respectively. Nonlinear effects can influence the predicted background fluctuations on even larger scales, up to few comoving Mpc (corresponding to few hundred kHz frequency bandwidths and 1-10 arc min beams), even if these scales are still not strongly nonlinear. Additionally, rare halos are always more strongly clustered than the underlying density distribution (i.e. the bias is > 1), again bringing nonlinear issues to the fore.

In order to address these important issues we have carried out a series of high-redshift N-body simulations of small scale structure formation, which we use to construct 21-cm line radio maps that illustrate the expected fluctuations in the emission. As no current simulations are able to span the full dynamic range relevant to 21-cm emission, however, we extend our results by developing a new formalism for calculating the nonlinear Eulerian bias of halos, which is based on the Lagrangian bias formalism of Scannapieco & Barkana (2002, hereafter SB02). We describe this approach in detail in this paper, verify it by comparing it with the results of our N-body simulations, and apply it to calculate improved predictions for the fluctuations in the 21-cm emission. These are then compared to the predictions given in Iliev et al. (2002), quantifying the impact of nonlinear effects on minihalo emission.

The structure of this work is as follows. In § 2 we describe a set of simulations of minihalo emission at high redshift, and use these to construct simulated maps at small angular scales. In § 3 we present our improved calculation of the Eulerian bias and verify it by comparison with the numerical simulations presented in § 2. In § 4 we modify the calculation of the radiation background from minihalos to incorporate the contribution due to nonlinear clustering of sources, according to the formalism described in § 3, and describe the results of our nonlinear formalism. Conclusions are given in § 5.

2 NUMERICAL SIMULATIONS

We simulated the formation of minihalos in three cubic computational volumes of comoving size 1 Mpc, 0.5 Mpc, and 0.25 Mpc, respectively. We used a standard Particle-Particle/Particle-Mesh (P^3M) algorithm (Hockney & Eastwood 1981), with 128^3 equal-mass particles, a 256^3 PM grid, and a softening length of 0.3 grid spacing. Here and throughout this paper we consider a flat Λ CDM model with density parameter $\Omega_0 = 0.3$, cosmological constant $\lambda_0 = 0.7$, Hubble constant $H_0 = 70 \text{ km s}^{-1} \text{ Mpc}^{-1}$, baryon density parameter $\Omega_b = 0.02 h^{-2}$ (where $h = H_0/100 \text{ km s}^{-1} \text{ Mpc}^{-1}$), and no tilt. The initial conditions were generated using the transfer function of Bardeen et al. (1986) with the normalization of Bunn & White (1997) (for details, see Martel & Matzner 2000, §2). All simulations started at redshift $z = 50$ and terminated at redshift $z = 9$. To identify minihalos, we used a standard friends-of-friends algorithm with a linking length equal to 0.25 times the mean particle spacing (see eg. Davis et al. (1985)). We rejected halos composed of 20 particles or less. Table 1 lists the comoving size L_{box} of the box, the comoving value of the softening length η , the total mass M_{tot} inside the box, and the particle mass M_{part} .

Here and throughout this paper, the 21-cm fluxes from individual minihalos are obtained as described in Paper I, by modeling the halos as Truncated Isothermal Spheres (Shapiro, Iliev & Raga 1999; Iliev & Shapiro 2001) and solving the radiative transfer equation self-consistently through each halo to obtain the line-integrated flux.

2.1 Simulated 21-cm radio maps

In Paper I, we computed the beam-averaged differential antenna temperature $\overline{\delta T_b}$ using

Table 1. Parameters of the N-body simulations

L_{box} (Mpc)	η (kpc)	$M_{\text{tot}}(M_{\odot})$	$M_{\text{part}}(M_{\odot})$
1.0	1.172	4.079×10^{10}	1.945×10^4
0.5	0.586	5.099×10^9	2.431×10^3
0.25	0.293	6.374×10^8	3.039×10^2

Figure 1 is supplied in jpg format. Higher resolution version is available from authors upon request.

Figure 1. (upper panels) Differential brightness temperature radio map of the 21-cm emission from minihalos at $z = 9$, produced as described in the text from Λ CDM N-body simulation of: (upper left panel) box size 1 Mpc and beam size $\Delta\theta_{\text{beam}} = 4''$, and (upper right panel) box size 0.5 Mpc and beam size $\Delta\theta_{\text{beam}} = 2''$. (lower left panel) box size 0.25 Mpc and $\Delta\theta_{\text{beam}} = 1''$, and (lower right panel) box size 0.25 Mpc and $\Delta\theta_{\text{beam}} = 0.25''$.

$$\overline{\delta T_b} = \frac{c(1+z)^4}{\nu_0 H(z)} \int_{M_{\text{min}}}^{M_{\text{max}}} \Delta\nu_{\text{eff}} \delta T_{b,\nu_0} A \frac{dn}{dM} dM, \quad (1)$$

where dn/dM is the mass function of minihalos, determined using the Press-Schechter approximation (Press & Schechter 1974), ν_0 is the rest-frame line frequency, $\Delta\nu_{\text{eff}}$ is the effective line width, $\delta T_{b,\nu_0}$ is the line-center differential brightness temperature, and A is the geometric cross-section of the halo. Since dn/dM does not contain information about the spatial distribution of minihalos, equation (1) can be used to compute the average temperature on the sky, but not its angular distribution. However, the N-body simulations provide us with the spatial distribution of minihalos, which we can use to compute simulated radio maps.

We assume that one face of the the computational volume at $z = 9$ is oriented toward the observer. Our goal is to compute the observed temperature on that face. The angular size of the map is given by $A_{\text{map}} = [L_{\text{box}}/(1+z)]/D_A(z)$, where L_{box} is the comoving size of the computational volume, and $D_A(z)$ is the angular diameter distance, which is equal to 921.03 Mpc at $z = 9$ for the Λ CDM model we consider. This gives $A_{\text{map}} = 22.395(L_{\text{box}}/1 \text{ Mpc})$ arc seconds. We then rewrite equation (1) as

$$\overline{\delta T_b}(\mathbf{x}) = \frac{c(1+z)^4}{\nu_0 H(z)} \left[\frac{\sum_i (\Delta\nu_{\text{eff}})_i (\delta T_{b,\nu_0})_i A_i w_i(\mathbf{x})}{\text{Volume}(\text{beam})} \right], \quad (2)$$

where \mathbf{x} is a particular location on the map (a “pixel”), “beam” is a cylinder of angular diameter $2R$ centered around the line of sight going through \mathbf{x} , whose depth is equal to the size of the computational volume, and the sum is over all minihalos. In general, for a cylinder of comoving radius R and comoving length L , these are related to the angular beam size and observational frequency bandwidth by $R = \Delta\theta_{\text{beam}}(1+z)D_A(z)/2$, and $L \approx (1+z)cH(z)^{-1}(\Delta\nu/\nu)_{\text{obs}}$. Notice that since dn/dM in equation (1) is in units of comoving volume, the volume of the beam in equation (2) is also comoving.

The quantity $w_i(\mathbf{x})$ is a weight that measures the contribution of minihalo i to the temperature at location \mathbf{x} . The simplest approach is to set $w_i = 1$ if the minihalo i is located inside the beam, and $w_i = 0$ otherwise. This would correspond to a top-hat filtering. However, it is more natural to assume that the contribution of a particular minihalo to a particular pixel varies smoothly with the location of the minihalo. Hence, it is preferable to use a Gaussian filter,

$$w_i(\mathbf{x}) = \frac{1}{2} e^{-(\mathbf{x}-\mathbf{x}_i)^2/2R^2}, \quad (3)$$

where \mathbf{x}_i is the angular position of the minihalo i . This filter is normalized such that $\iint w_i(\mathbf{x}) d^2x = \pi R^2$, the area of the top-hat filter. Equation (2) reduces to

$$\overline{\delta T_b}(\mathbf{x}) = \frac{c(1+z)^4}{2\nu_0 H(z)} \frac{1}{\pi R^2 L_{\text{box}}} \sum_i (\Delta\nu_{\text{eff}})_i (\delta T_{b,\nu_0})_i A_i e^{-(\mathbf{x}-\mathbf{x}_i)^2/2R^2}, \quad (4)$$

where $\pi R^2 L_{\text{box}}$ is the comoving volume of the beam. The resulting maps are shown in Figure 1. Due to the small box sizes that are required to resolve the minihalos, the beam sizes used to produce the maps are also very small, ranging from $4''$ to $0.25''$. The fluxes from such small beam sizes are well below the sensitivity limits of the currently planned radio arrays LOFAR and SKA. Additionally, the larger-box (1 Mpc and 0.5 Mpc) simulations do not have sufficient mass resolution to resolve the smallest halos, while the larger-mass minihalos are not present in the smaller box simulations. Therefore the flux levels are somewhat underestimated in all cases, and unless much larger radio arrays are developed in the future, and until much larger simulations are performed, these maps should be considered only as illustrative of fluctuations on very small scales rather than a guide for observers.

3 NONLINEAR CLUSTERING REGIME AND COMPARISON TO SIMULATIONS

3.1 An analytic approach to nonlinear clustering

As our simulations are unable to span a sufficient range of scales to accurately resolve minihalos and reproduce the physical scales accessible to observations simultaneously, we adopt instead an alternate technique to estimate the full nonlinear signal. Here we make use of an approximate formalism that is an extension of the one developed in Scannapieco & Barkana (2002). A more complete discussion of this method, refinement of the basic formalism, and detailed comparisons with simulations will be presented in a separate paper. In this section we summarize the basic features of this approach and show that it is sufficient for our purposes in this investigation.

In SB02 the authors extended the Press-Schechter formalism as reinterpreted by Bond et al. (1991) to calculate the number density of collapsed objects in two regions of space initially separated by a fixed comoving distance. In the Press-Schechter approach the presence of a virialized halo is associated with a density peak in a linear treatment that falls above a critical value, taken from the collapse of a spherical top-hat perturbation. At the moment at which such a spherical perturbation virializes, the overdensity predicted by linear theory is $\delta_c = 1.686$ (Peebles 1980) in the Einstein-de Sitter model, where the linear overdensity field is defined as $\delta(\mathbf{x})D^{-1}(z) \equiv \rho(\mathbf{x}, z)/\bar{\rho}(z) - 1$, where $\rho(\mathbf{x})$ is the linear mass density as a function of position and $\bar{\rho}$ is the mean mass density. Note that in this approach the linear overdensity field $\delta(\mathbf{x})$ is described in terms of its value extrapolated to $z = 0$, and its evolution with time is subsumed by the “linear growth factor” $D(z) = \delta(0)/\delta(z)$.

In this picture the presence of a halo can be associated with a random walk procedure. At a given redshift we consider the smoothed density in a region around a point in space. We begin by averaging over a large mass scale M , or equivalently, by including only small comoving wavenumbers k . We then lower M , adding k modes, and adjusting $\delta(M)$ accordingly. This amounts to a random walk in which the “time variable” is the variance associated with the filter mass and the “spatial variable” is the overdensity itself. This walk continues until we find the highest value for which the averaged overdensity is higher than $\delta_c D^{-1}(z)$ and assume that the point belongs to a halo with a mass M corresponding to this filter scale.

The problem of halo collapse at two positions in space can be similarly associated with two random walks in the presence of a barrier of height $\delta_c D^{-1}(z)$. These random walks are extremely correlated at large scales, and become less and less so as the modes of smaller and smaller scales are added. In SB02 this process was approximated by a completely correlated random walk down to an overall variance $S = \xi$, where ξ is the correlation function that accounts for the excess probability of finding a second halo at a fixed distance from a given halo. This correlated random walk was then followed by uncorrelated walks down to the final variances associated with the masses of the objects, $S = \sigma^2(M_1)$ and $\sigma^2(M_2)$.

This procedure lends itself directly to calculating the overall increase in number density due to infall. The fact that the overdensity on large scales will contract the distances between halos provides an additional contribution at the scale $\sigma^2(x) = \xi$, the scale down to which the evolution of the two points is completely correlated. Let us call the linear overdensity at redshift zero at this scale δ_0 . The probability distribution of this value is then simply given by a Gaussian, with a barrier imposed at $\nu(z) \equiv \delta_c D^{-1}(z)$. In this case,

$$Q_0(\nu, \delta_0, \xi) = [G(\delta_0, \xi) - G(2\nu - \delta_0, \xi)] \theta(\nu - \delta_0), \quad (5)$$

where Q_0 is the probability distribution function of δ_0 , $G(\delta, \xi) \equiv (2\pi\xi)^{-1/2} e^{-\delta^2/2\xi}$, and θ is the Heaviside step function.

With this expression in hand, we now consider $f_2(\nu(z), \sigma_1^2, \sigma_2^2, \delta_0, \xi) d\sigma_1^2 d\sigma_2^2$, the joint probability of having point A in a halo with mass corresponding to the range σ_1^2 to $\sigma_1^2 + d\sigma_1^2$ and point B in a halo with mass corresponding to the range σ_2^2 to $\sigma_2^2 + d\sigma_2^2$, whose random walks pass through a value of δ_0 at the $\sigma^2(M) = \xi$ scale. In this case we obtain an expression analogous to equation (37) of SB02

$$f_2(\nu(z), \delta_0, \sigma_1^2, \sigma_2^2, \xi(r)) = \frac{\partial}{\partial \sigma_1^2} \frac{\partial}{\partial \sigma_2^2} \left[2 \int_{-\infty}^{\nu(z)} d\delta_1 - \int_{-\infty}^{\infty} d\delta_1 \right] \left[2 \int_{-\infty}^{\nu(z)} d\delta_2 - \int_{-\infty}^{\infty} d\delta_2 \right] Q_{12}(\nu, \delta_1, \delta_2, \sigma_1^2, \sigma_2^2, \xi(r)), \quad (6)$$

where now $Q_{12} \equiv G(\delta_1 - \delta_0, \sigma_1^2 - \xi) G(\delta_2 - \delta_0, \sigma_2^2 - \xi)$, and the reader is referred to SB02 for a more detailed derivation of f_2 from the underlying probability distribution.

Averaging equation (6) over the probability distribution for δ_0 as given in equation (5) and carrying out the partial derivatives we obtain the Eulerian “bivariate” number density, the joint probability of having point A lie in a halo in the mass range M_1 to $M_1 + dM_1$ and point B at a comoving distance r lie in a halo in the mass range M_2 to $M_2 + dM_2$ at a redshift z :

$$\frac{d^2 n_{12,E}^2(r, z)}{dM_1 dM_2} = \frac{\bar{\rho}}{M_1} \left| \frac{d\sigma_1^2}{dM_1} \right| \frac{\bar{\rho}}{M_2} \left| \frac{d\sigma_2^2}{dM_2} \right| \left(1 - \frac{\partial \xi}{\partial \sigma_1^2} \right) \left(1 - \frac{\partial \xi}{\partial \sigma_2^2} \right) f_{2,E}(\nu(z), \sigma_1^2, \sigma_2^2, \xi(r)), \quad (7)$$

where

$$f_{2,E}(\nu, \sigma_1^2, \sigma_2^2, \xi) \equiv \int_{-\infty}^{\nu} d\delta_0 Q_0(\delta_0, \xi) g(D^{-1}\delta_0) f(\nu - \delta_0, \xi - \sigma_1^2) g(D^{-1}\delta_0) f(\nu - \delta_0, \xi - \sigma_2^2), \quad (8)$$

and $f(\nu, \sigma^2) \equiv (2\pi)^{-1/2} (\nu/\sigma^3) e^{-\nu^2/2\sigma^2}$. Here $g(D^{-1}\delta_0)$ is $\rho/\bar{\rho}$ at scale at which the points A and B are completely correlated.

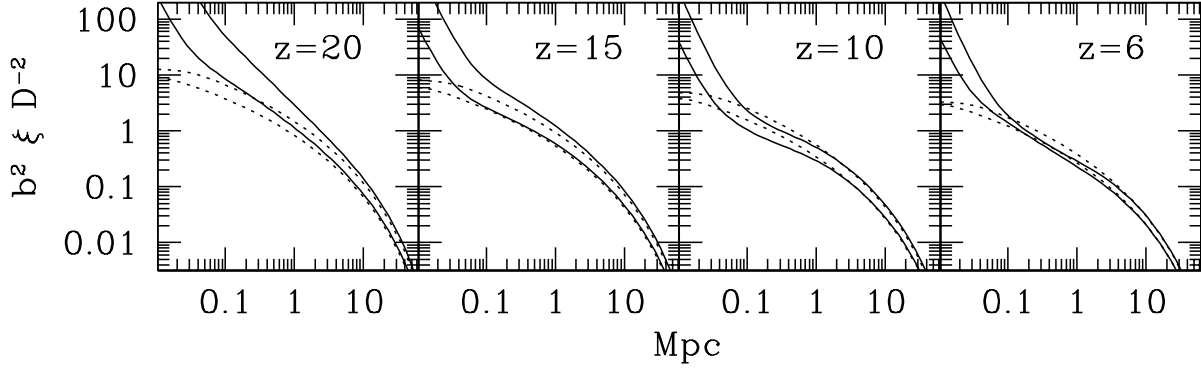


Figure 2. Comparison of standard and nonlinear bias. In all panels, the solid curves give $b^2 D^{-2} \xi$ as calculated in equation (11) while the dotted lines give the standard bias expressions as used in Paper I. For each case, the upper curves assume a fixed mass of $10^7 M_\odot$, corresponding to a spherical perturbation with a comoving radius of approximately 38 kpc, while the lower curves assume a fixed mass of $10^6 M_\odot$, corresponding to a comoving radius of 18 kpc.

This can be thought of as the contraction of a large spherical perturbation that surrounds both points and contains a total mass M of material, where $\sigma^2(M) = \xi$. This contribution is then just $(1 + D^{-1} \delta_0)$ in the linear regime, but when $D^{-1} \delta_0$ becomes larger this quantity grows much more quickly. For our purposes here we assume $g(D^{-1} \delta_0) = (1 + D^{-1} \delta_0)$ for all values as this will prove sufficient to reproduce the simulated results.

Finally we define the Eulerian bias as

$$b_E^2 \xi D^{-2} \equiv \frac{d^2 n_{12,E}^2}{dM_1 dM_2} \left(\frac{dn_{1,E}}{dM_1} \frac{dn_{2,E}}{dM_2} \right)^{-1} - 1 \quad (9)$$

where we divide by dn_E/dM , a single point number density that accounts for the self correlations between the collapsed peaks and the overdense sphere, which are over-counted in equation (7). To compute this probability we again carry out an average over the probability distribution (5), but in this case we consider $f_1(\nu, \delta_0, \sigma_1^2) d\sigma_1^2 = f(\nu - \delta_0, \sigma^2 - \xi) d\sigma_1^2$, the probability of having a single point in a halo with a mass corresponding to the range σ_1^2 to $\sigma_1^2 + d\sigma_1^2$ whose random walk passes through δ_0 at the $\sigma^2(M) = \xi$ scale. This gives $dn_E/dM = (\bar{\rho}/M) |d\sigma^2/dM| (1 + \partial \xi / \partial \sigma^2) f_E(\nu, \sigma^2)$ where

$$f_E(\nu, \sigma^2, \xi) \equiv \int_{-\infty}^{\nu} d\delta_0 Q_0(\delta_0, \nu, \xi) g(\delta_0 D^{-1}) f(\nu - \delta_0, \xi - \sigma^2). \quad (10)$$

Combining these expressions yields

$$b_E^2 \xi D^{-2} = \frac{f_{2,E}(\nu, \sigma_1^2, \sigma_2^2, \xi)}{f_E(\nu, \sigma_1^2, \xi) f_E(\nu, \sigma_2^2, \xi)} - 1, \quad (11)$$

which is our final expression for the bias.

Note that at large distances we can work to order δ_0^2 to determine the asymptotic limit as $\xi/\sigma^2 \rightarrow 0$. In this limit

$$g(\delta_0 D^{-1}) f(\nu - \delta_0, \sigma^2 - \xi) \rightarrow \left[1 - D^{-1} \delta_0 \left(\frac{\nu^2}{\delta_c \sigma^2} - \frac{1}{\delta_c} + 1 \right) + \mathcal{O}(\delta_0^2) \right] f(\nu, \sigma^2 - \xi), \quad (12)$$

and the only surviving term in equation (11) is the cross term between terms of order δ_0 . All other terms cancel out between the numerator and the denominator, giving

$$b_E^2 = \left(1 + \frac{\nu/\sigma_1^2 - 1}{\delta_c} \right) \left(1 + \frac{\nu/\sigma_2^2 - 1}{\delta_c} \right), \quad (13)$$

which is the usual limit as in Mo & White (1996). Thus our formalism reproduces the usual bias at large distance, as was used in Paper I.

3.2 Nonlinear properties and comparisons with simulations

In Fig. 2 we plot $b_E^2 \xi D^{-2}$ as calculated from equation (11) and the standard expression, equation (13), using the fit to the density fluctuation power spectrum given by Eisenstein & Hu (1999). In each panel we show the behavior of $10^7 M_\odot$ and $10^6 M_\odot$ objects at four different redshifts, which span the detectable range. At large distances, the linear and nonlinear clustering expressions approach each other asymptotically, as expected from equation (13). On the other hand, the solid lines shoot up

dramatically at the smallest distances. This is because the separation between the halos is comparable to their radii, and thus the likelihood of finding a second collapsed halo at the same point becomes infinite as $r \rightarrow 0$.

At intermediate distances the behavior is more complex. For relatively rare objects, corresponding to high redshifts, the nonlinear values consistently exceed the standard ones. For example, at a distance of 0.1 comoving Mpc, the nonlinear $10^7 M_\odot$ value is almost twice that of the standard result at $z = 20$, while it is only about 70% of the standard result at $z = 6$.

To compare this behavior with numerical results, we calculated the correlations between halos for each of our simulations. In this case $b^2 \xi D^{-2}$ is directly comparable to the *halo* correlation function $\xi_{i,i}(r)$, the excess probability of finding two particles within a mass bin m_i separated by a distance r . Here we define $\langle N(r) \rangle$ as the mean number of particles within a distance R of a given particle, averaged over all particles. $\langle N(r) \rangle$ is then given by,

$$\langle N_{i,i}(r) \rangle = \frac{4\pi r^3 n_i}{3} + 4\pi n_i \int_0^r \xi_{i,i}(r') r'^2 dr', \quad (14)$$

where n_i is the number density of particles within a mass bin i . We compute $\langle N_{i,i}(r) \rangle$ by counting particle pairs in radial bins, and differentiate to get $\xi_{i,i}(r)$.

Similarly, the cross correlation, $\xi_{i,j}(r)$ is defined as the excess probability of finding a particle within a mass bin m_i and a particle within a mass bin m_j separated by a distance r . This expression is symmetric, so that $\xi_{i,j}(r) = \xi_{j,i}(r)$. We define $\langle N_{i,j}(r) \rangle$ as the mean number of particles in a mass bin m_j , located within a radius R of a particle in a mass bin m_i , averaged over all particles of mass m_i . This is given by

$$\langle N_{i,j}(r) \rangle = \frac{4\pi r^3 n_j}{3} + 4\pi n_j \int_0^r \xi_{i,j}(r') r'^2 dr', \quad (15)$$

where n_j is the number density of particles within mass bin j . Notice that $n_j = N_j/V_{\text{box}}$, where N_j is the number of particles of mass m_j and V_{box} is the volume of the box, and that $\langle N_{i,j}(r) \rangle$ is obtained by dividing the total number of pairs with separation $r' < r$, by the number N_i of i particles. Thus we can rewrite equation (15) as

$$N_{i,j}(< r) = \frac{4\pi N_i N_j}{3V_{\text{box}}} \left[r^3 + 3 \int_0^r \xi_{i,j}(r') r'^2 dr' \right], \quad (16)$$

which is clearly symmetric in i and j .

Using these definitions we examined the distribution of halos in each of our simulations at $z = 15$ and $z = 9$. In each case we divided the halos into mass bins of roughly equal size and compared their correlations to those given by equation (11). In the left panels of Fig. 3 we compare the mass averaged correlation between halos,

$$\left(\int_{m_i} \frac{dn}{dM_i} \int_{m_j} \frac{dn}{dM_j} b_E^2 \xi D^{-2} \right) \left(\int_{m_i} \frac{dn}{dM_i} \int_{m_j} \frac{dn}{dM_j} \right)^{-1}, \quad (17)$$

to the numerical value, $\xi_{i,j}$, for objects of mass scales $4.08 \times 10^5 M_\odot \leq m_1 \leq 5.45 \times 10^5 M_\odot$, $5.64 \times 10^5 M_\odot \leq m_2 \leq 1.03 \times 10^6 M_\odot$, and $1.05 \times 10^6 M_\odot \leq m_3 \leq 7.73 \times 10^7 M_\odot$ in our 1 Mpc³ simulation at $z = 15$. There were 595, 607 and 484 objects in each of these mass bins respectively, while the Press-Schechter approximation predicts 506, 637, and 604. Here the error bars are $2\text{-}\sigma$ estimates of the statistical noise given by $2\xi_{i,i}(r)/\sqrt{N_{i,i}(< R)}$.

For all mass ranges, there is a good match between the numerical $\xi_{i,i}$ and our analytic expression, with both values equaling or exceeding the linear predictions at most distances. The only values at which the predictions of the simulations fall below equation (13) in fact, is at large distances, for which the separations between halos begin to approach the simulation box size, and some damping is to be expected. Similar comparisons with our smaller box simulations yielded comparable results, but with larger damping at these distances, indicating that the analytic and simulated correlations are a good match at all reliable separations.

On the other hand, the cross-correlation functions are much poorer match, particularly if the mass bins are very different, such as in the m_1 and m_3 case. For all correlations however, our nonlinear estimate falls between the standard and simulated results, indicating that the correlations between halos exceed those predicted by equation (13), and that our approach gives a conservative estimate of this excess.

In the right panels of Fig. 3, we compare the mass-averaged correlation between halos to numerical results obtained with our 1 Mpc³ simulation at $z = 9$. In this case, we divided our halos into five mass bins, three of which are shown in this figure. For these bins, $4.08 \times 10^5 M_\odot \leq m_1 \leq 4.67 \times 10^5 M_\odot$, $6.23 \times 10^5 M_\odot \leq m_3 \leq 8.17 \times 10^5 M_\odot$, and $1.32 \times 10^6 M_\odot \leq m_5 \leq 3.44 \times 10^6 M_\odot$, and we found 589, 572, and 596 halos in them respectively, while the Press-Schechter approximation predicts 520, 640, and 690. In this case there is good agreement between the correlations and cross-correlations obtained from the simulations and our nonlinear estimates, for all mass scales considered, and they all have the same dependence on distance. In fact the analytical estimates are consistent with the results of the simulations for all distances that are small relative to the box, apart from the drop at small distances in the $m_1 m_1$ case, which is most likely due to small-number statistics. Note that unlike the higher

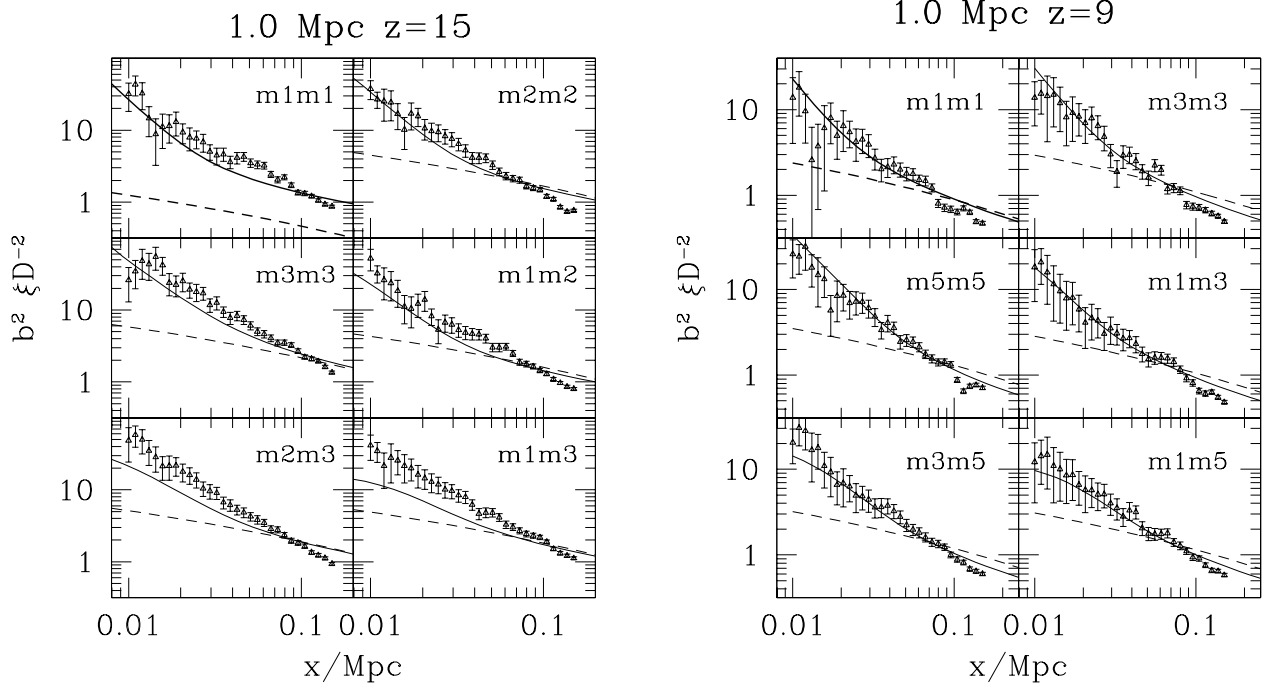


Figure 3. Comparison between nonlinear analytic expressions for the bias and simulations at two different redshifts. In the left panels $z = 15$ and the halo are divided into three mass bins: $4.08 \times 10^5 M_\odot \leq m_1 \leq 5.45 \times 10^5 M_\odot$, $5.64 \times 10^5 M_\odot \leq m_2 \leq 1.03 \times 10^6 M_\odot$, and $1.05 \times 10^6 M_\odot \leq m_3 \leq 7.73 \times 10^7 M_\odot$. In the right panels $z = 9$ and halos are divided into five mass bins, three of which are shown: $4.08 \times 10^5 M_\odot \leq m_1 \leq 4.67 \times 10^5 M_\odot$, $6.23 \times 10^5 M_\odot \leq m_3 \leq 8.17 \times 10^5 M_\odot$, and $1.32 \times 10^6 M_\odot \leq m_5 \leq 3.44 \times 10^6 M_\odot$. In both cases, the points are the correlation function as calculated from the simulations, while the solid lines give our analytic estimates as given by equation (11). Finally, the dashed lines give correlations as estimated from the standard approach, equation (13).

redshift case, our nonlinear estimates now fall below the standard analytic approach at larger distances, as we saw in the lower redshift cases in Fig. 2.

Finally, we define the flux-averaged correlation between objects,

$$\bar{b}_E^2 \xi D^{-2} = \frac{\int dM_1 \int dM_2 F(M_1) (dn/dM_1) F(M_2) (dn/dM_2) b_E^2 \xi D^{-2}}{[\int dM F(M) (dn/dM)]^2}, \quad (18)$$

where $F(M)$ is the line-integrated flux for minihalo of mass M . We use this expression below for computing the nonlinear fluctuation of the 21-cm emission from minihalos.

4 FLUCTUATIONS OF THE 21-CM EMISSION FROM MINIHALOS: EFFECTS OF THE NONLINEAR BIAS

The amplitude of $q\sigma$ (i.e. q times the rms value) angular fluctuations in the differential brightness temperature δT_b (or, equivalently, of the flux) in the linear regime are given by

$$(\delta T_b^2)^{1/2} = qb(z) \sigma_p \overline{\delta T_b} \quad (19)$$

(Iliev et al. 2002), where $b(z)$ is the mean flux-weighted bias, and

$$\sigma_p^2 = \frac{8D^{-2}(z)}{\pi^2 L^2 R^2} \int_0^\infty dk \int_0^1 dx \frac{\sin^2(kLx/2) J_1^2[kR(1-x^2)^{1/2}]}{x^2(1-x^2)} (1+f x^2)^2 \frac{P(k)}{k^2}, \quad (20)$$

where $P(k)$ is the linear power spectrum at $z = 0$, and the factor $(1+f x^2)^2$, where $f \approx [\Omega(z)]^{0.6}$ is the correction to the cylinder length for the departure from Hubble expansion due to peculiar velocities (Kaiser 1987). In order to apply the formalism developed in §3, we use the fact that the power spectrum $P(k)$ is the Fourier transform of the correlation function $\xi(r)$:

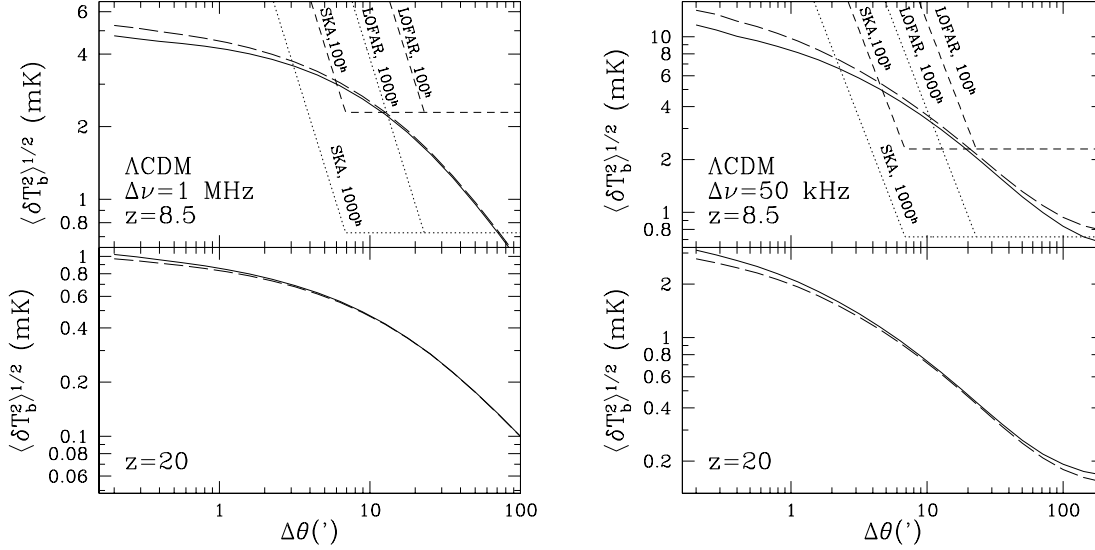


Figure 4. Predicted 3- σ differential antenna temperature fluctuations at $z = 8.5$ and $z = 20$ vs. angular scale $\Delta\theta_{\text{beam}}$ for standard ΛCDM model for observer frequency bandwidths $\Delta\nu_{\text{obs}} = 1$ MHz (left panels) and $\Delta\nu_{\text{obs}} = 50$ kHz (right panels): using Mo & White bias (long-dashed curves) and SB02 (solid curves). Also indicated is the predicted sensitivity of LOFAR and SKA integration times of 100 h (short-dashed lines) and 1000 h (dotted lines), with compact sub aperture (horizontal lines) and extended configuration needed to achieve higher resolution (diagonal lines) (see <http://www.lofar.org/science> and Paper I for details).

$$P(k) = \int d^3r \xi(r) e^{-i\mathbf{k}\cdot\mathbf{r}} \quad (21)$$

This allows us to obtain

$$\sigma_p^2 = \frac{32D^{-2}(z)}{\pi L^2 R^2} \int_0^\infty dr r^2 \xi(r) f(r, R, L), \quad (22)$$

where

$$f(r, R, L) \equiv \int_0^1 dx (1 + fx^2)^2 \int_0^\infty dk \frac{\sin(kr)}{kr} \frac{\sin^2(kLx/2)}{x^2} \frac{J_1^2[kR(1-x^2)^{1/2}]}{k^2(1-x^2)}. \quad (23)$$

Using equations (22) and (19) the mean squared angular fluctuations become

$$\langle \delta T_b^2 \rangle = \left(\frac{32}{\pi L^2 R^2} \right)^2 \int_0^\infty dr r^2 [D^{-2}b^2(z)\xi(r)(\overline{\delta T_b})^2] f(r, R, L). \quad (24)$$

We apply the formalism developed in §3 by simply replacing the expression $[D^{-2}b^2(z)\xi(r)(\overline{\delta T_b})^2]$ above with the corresponding expression $D^{-2}\overline{b_E^2}\xi(r)(\overline{\delta T_b})^2$ for the mean Eulerian flux-weighted bias calculated in §3. As shown above, at very large distances the two expressions are equivalent, but at smaller distances the new formalism is much better at reproducing the numerical results.

Illustrative results for 3- σ fluctuations at redshifts $z = 8.5$ and $z = 20$ vs. the beam size $\Delta\theta_{\text{beam}}$ for fixed observed frequency bandwidths $\Delta\nu_{\text{obs}} = 1$ MHz and 50 kHz are shown in Fig. 4 along with the results obtained using the linear bias in order to facilitate comparison. The approximate sensitivities for LOFAR and SKA radio arrays are also shown where appropriate (see Paper I for details), but here we concentrate on the differences between the results from the two approaches and the robustness of our original predictions rather than observability, which was discussed in Paper I. As expected, if both $\Delta\theta_{\text{beam}}$ and $\Delta\nu_{\text{obs}}$ are large (Fig. 4, left panels) the current results are largely indistinguishable from the results from Paper I, since at such large scales the bias calculated in §3 reduces to the linear expression as shown by equation (13). If one or both of $\Delta\theta_{\text{beam}}$ and $\Delta\nu_{\text{obs}}$ is reduced, differences between the two results grow, becoming as large as 20–30%, particularly for small $\Delta\nu_{\text{obs}}$ (Fig. 4, right panels). At redshifts $z \lesssim 15$ using the linear bias gives somewhat of an overestimate of the results, although a small one compared to the various uncertainties of the calculation, while at higher redshifts using the linear bias gives a noticeable underestimate of the fluctuations. The two results hardly differ in the observable range, however, regardless of the value of $\Delta\nu_{\text{obs}}$.

In Fig. 5 we plot the 3- σ fluctuations at redshifts $z = 8.5$ and $z = 20$ vs. the observer frequency bandwidth $\Delta\nu_{\text{obs}}$ for fixed beam sizes $\Delta\theta_{\text{beam}} = 1'$ and $20''$. We have chosen such small beam sizes in order to investigate the upper limit of the deviation of the results due to the nonlinear clustering of halos. Again, the same patterns emerge, the linear bias approach

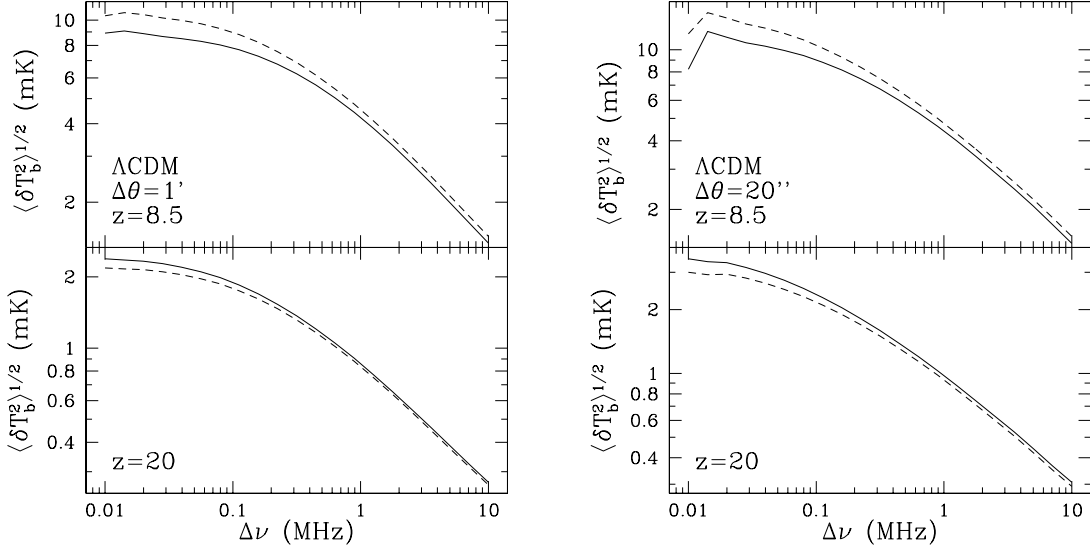


Figure 5. Predicted 3- σ differential antenna temperature fluctuations at $z = 8.5$ and $z = 20$ at small angular scales vs. observer frequency bandwidth $\Delta\nu_{\text{obs}}$ for standard Λ CDM model and for angular scales $\Delta\theta = 1'$ (left panels) and $\Delta\theta = 20''$ (right panels): using standard linear bias (dashed curves) and nonlinear bias (solid curves).

overestimates the fluctuations at the lower end of the range of considered redshifts by up to 20-30 %, particularly for small $\Delta\nu_{\text{obs}}$, and underestimates the fluctuations at the higher redshifts by a similar fraction.

5 CONCLUSIONS

We have developed a new analytical method for estimating the nonlinear bias of halos and used it to calculate the fluctuations of the 21-cm emission from the clustering of high- z minihalos. This method is likely to be useful in tackling a much wider range of problems that lie beyond the capabilities of current numerical simulations, and will be refined and further verified in a future publication. The minihalo bias predicted by our method at large scales reproduces the linear bias, as derived in Mo & White (1996), and is much larger at small scales, confirming naive expectations. At intermediate scales, however, its behavior is more complex and both mass- and redshift-dependent. For very rare halos at high- z (roughly $z > 15$), the standard linear bias is lower than our nonlinear prediction at all length scales. At the lower end of the redshift range we consider (down to $z = 6$) the linear bias is higher at intermediate scales (few hundred kpc to few Mpc comoving) and lower at smaller scales.

We have also compared the predictions our new method with the results of N-body numerical simulations, which we used both to verify our approach and to produce sample radio maps. Due to the limited dynamical range of our simulations, however, these maps are only illustrative of the behavior of the fluctuations on very small scales, below the sensitivity limits of LOFAR and SKA. On the scales at which the simulations are reliable, we find excellent agreement between these results and our analytical approach. The most significant discrepancies occur in the calculation of cross-correlation functions of very different mass bins at higher redshifts. However, even these departures are relatively modest, and in all cases our method reproduces the simulation results significantly better than the linear bias.

Despite these differences, we find our original linear bias predictions for the fluctuations of the 21-cm emission from minihalos to be very robust at the scales and frequencies corresponding to observable signals. The prediction using the flux-weighted nonlinear bias never departs from the linear prediction by more than few percent in that range, well within the other uncertainties of the calculation. This robustness is partly accidental, however, and is due to the nonlinear bias varying above and below the linear one depending on the length scale, leading to partial cancellation of the differences when the correlation function is integrated over the length scales.

For small observational bandwidths, $\Delta\nu_{\text{obs}}$, there is less cancellation and the differences in the two predictions grow at all beam sizes, $\Delta\theta_{\text{beam}}$. Similarly, if $\Delta\theta_{\text{beam}}$ is very small, there is little cancellation, and the discrepancies are larger at all bandwidths. In these cases the linear bias gives an overestimate of the 21-cm emission fluctuations from minihalos at the low end of the redshift range, and an underestimate at high- z , even at large values of $\Delta\nu_{\text{obs}}$. However, when both the beam size and the frequency bandwidth are large the differences in the two approaches at small scales are diluted, and the resulting 21-cm emission fluctuations become identical.

Finally, we predict that an important strategy for improving the chances for detection is to decrease the observational

frequency bandwidth $\Delta\nu_{\text{obs}}$. As long as $\Delta\nu_{\text{obs}}$ and the beam size $\Delta\theta_{\text{beam}}$ are large enough to provide fair sample of the halo distribution, the mean 21-cm flux is independent of $\Delta\nu_{\text{obs}}$, while the fluctuations grow as $\Delta\nu_{\text{obs}}$ decreases. For example, if $\Delta\nu_{\text{obs}} = 50$ kHz is used, as compared to $\Delta\nu_{\text{obs}} = 1$ MHz, the expected signal is increased by factor of ~ 2 . Thus it may be through a narrow frequency window that astronomers get their first glimpses of the cosmological Dark Ages.

ACKNOWLEDGMENTS

We would like to thank Andrea Ferrara and Rennan Barkana for useful comments and discussions. This work was supported in part by the Research and Training Network “The Physics of the Intergalactic Medium” set up by the European Community under the contract HPRN-CT2000-00126 RG29185, NASA grants NAG5-10825 and NAG5-10826 to PRS, and Texas Advanced Research Program 3658-0624-1999 to PRS and HM. ES has been supported in part by an NSF MPS-DRF fellowship.

REFERENCES

- Bardeen, J. M., Bond, J. R., Kaiser, N., & Szalay, A. S. 1986, *ApJ*, 304, 15
 Bond, J. R., Cole, S., Efstathiou, G., & Kaiser, N. 1991, *ApJ*, 379, 440
 Bunn, E. F., & White, M. 1997, *ApJ*, 480, 6
 Davis, M., Efstathiou, G., Frenk, C. S., & White, S. D. M. 1985, *ApJS*, 57, 241
 Eisenstein, D. J., & Hu, W. 1999, *ApJ*, 511, 5
 Hockney, R. W., & Eastwood, J. W. 1981, *Computer Simulation Using Particles* (New York: McGraw Hill)
 Hogan, C. J., & Rees, M. J. 1979, *MNRAS*, 188, 791
 Iliev, I. T., & Shapiro, P. R. 2001, *MNRAS*, 325, 468
 Iliev, I. T., Shapiro, P. R., Ferrara, A., & Martel, H. 2002 *ApJ*, 572, L123 (Paper I)
 Kaiser, N. 1987, *MNRAS*, 227, 1
 Madau, P., Meiksen, A., & Rees, M. J. 1997, *ApJ*, 475, 429
 Martel, H., & Matzner, R. 2000, *ApJ*, 530, 525
 Mo, H., & White, S. D. M. 1996, *MNRAS*, 282, 347
 Peebles, P. J. E. 1980, *The Large-Scale Structure of the Universe* (Princeton: Princeton University Press)
 Press, W. H., & Schechter, P. 1974, *ApJ*, 187, 425
 Scannapieco, E., & Barkana, R. 2002, *ApJ*, 571, 585 (SB02)
 Scott, D., & Rees, M. J. 1990, *MNRAS*, 247, 510
 Shapiro, P. R., Iliev, I. T., & Raga, A. C. 1999, *MNRAS*, 307, 203
 Shaver, P. A., Windhorst, R. A., Madau, P., & de Bruyn, A. G. 1999, *A&A*, 345, 390
 Subramanian, K., & Padmanabhan, T. 1993, *MNRAS*, 265, 101
 Tozzi, P., Madau, P., Meiksen, A., & Rees, M. J. 2000, *ApJ*, 528, 597

This figure "tempmap_0.25Mpc_1s.jpg" is available in "jpg" format from:

<http://arxiv.org/ps/astro-ph/0209216v1>

This figure "tempmap_0.5Mpc_2s.jpg" is available in "jpg" format from:

<http://arxiv.org/ps/astro-ph/0209216v1>

This figure "tempmap_1Mpc_4s.jpg" is available in "jpg" format from:

<http://arxiv.org/ps/astro-ph/0209216v1>

This figure "tempmap_0.25Mpc_0.25s.jpg" is available in "jpg" format from:

<http://arxiv.org/ps/astro-ph/0209216v1>